entropy

MDPI

Article

A Hybrid Domain Image Encryption Algorithm Based on Improved Henon Map

Yong Chen [1], Shucui Xie [2,*] and Jianzhong Zhang [3]

[1] School of Communication and Information Engineering, Xi'an University of Posts and Telecommunications, Xi'an 710121, China; 13253700106@163.com
[2] School of Science, Xi'an University of Posts and Telecommunications, Xi'an 710121, China
[3] School of Mathematics and Statistics, Shaanxi Normal University, Xi'an 710119, China; jzzhang@snnu.edu.cn
* Correspondence: xieshucui@163.com

Abstract: A hybrid domain image encryption algorithm is developed by integrating with improved Henon map, integer wavelet transform (IWT), bit-plane decomposition, and deoxyribonucleic acid (DNA) sequence operations. First, we improve the classical two-dimensional Henon map. The improved Henon map is called 2D-ICHM, and its chaotic performance is analyzed. Compared with some existing chaotic maps, 2D-ICHM has larger parameter space, continuous chaotic range, and more complex dynamic behavior. Second, an image encryption structure based on diffusion–scrambling–diffusion and spatial domain–frequency domain–spatial domain is proposed, which we call the double sandwich structure. In the encryption process, the diffusion and scrambling operations are performed in the spatial and frequency domains, respectively. In addition, initial values and system parameters of the 2D-ICHM are obtained by the secure hash algorithm-512 (SHA-512) hash value of the plain image and the given parameters. Consequently, the proposed algorithm is highly sensitive to plain images. Finally, simulation experiments and security analysis show that the proposed algorithm has a high level of security and strong robustness to various cryptanalytic attacks.

Keywords: image encryption; improved Henon map; integer wavelet transform; double sandwich structure; SHA-512

check for updates

Citation: Chen, Y.; Xie, S.; Zhang, J. A Hybrid Domain Image Encryption Algorithm Based on Improved Henon Map. *Entropy* **2022**, *24*, 287. https://doi.org/10.3390/e24020287

Academic Editor: Jose Santamaria

Received: 29 November 2021
Accepted: 15 February 2022
Published: 17 February 2022

1. Introduction

With the development of the information revolution, network technology has been rapidly popularized. As one of the critical carriers of information exchange in network technology, digital image plays an important role in our daily life, and its transmission security problem has been widely concerned. Therefore, digital image encryption arises at the historic moment. Image encryption can be used in application scenarios based on computer vision, such as medical vision [1–3], secure surveillance framework for Internet of Things [4], and biometrics [5]. While the digital image has the characteristics of large amount of data, high redundancy, and strong correlation between pixels [6], the encryption algorithms designed for text information, such as the Data Encryption Standard (DES) and Advanced Encryption Standard (AES), are unsuitable for image encryption scenarios [1,7].

In recent years, with the in-depth study of chaos theory, the unique properties of chaotic maps have been explored, such as pseudorandomness, ergodicity, nonperiodicity, and high sensitivity to initial values. These properties make the chaos-based image encryption algorithms can exhibit a good ability to protect image data. So far, the image encryption algorithms based on chaotic systems have been widely studied [8–16]. In [8], an image encryption algorithm based on random integer cycle shift and logistic map is proposed. Zhao et al. [9] proposed a dynamic block image encryption algorithm based on variable-length secret key and modified Henon map. Zhao et al. [10] proposed a chaotic encryption algorithm based on long short-term memory artificial neural networks (LSTM-ANN). In the proposed scheme, the chaotic sequence used in the encryption algorithm is constructed by the LSTM-ANN deep learning network. Chai et al. [11] proposed a chaotic encryption algorithm based on generative adversarial network (GAN), convolutional neural network (CNN), and denoising network. In the proposed algorithm, the deep learning reconstruction scheme based on GAN improves the robustness of the encryption algorith, and the CNN denoiser improves the visual expression of the decrypted image. In [12], a color image compression–encryption scheme based on autoencoder is proposed, where the encrypted image is losslessly compressed by unsupervised autoencoder deep learning networks and this can speed up the transmission. In [13], a chaotic encryption scheme based on genetic algorithm is proposed. Due to the inherent advantages such as high parallelism, huge information density, and ultralow energy consumption, deoxyribonucleic acid (DNA) computing attracts the attention of cryptographers. Therefore, various algorithms combining chaotic systems and DNA computing have been proposed. For instance, Wang et al. [17] proposed an image encryption algorithm based on a six-dimensional hyperchaotic system and DNA encoding. El-Shafai et al. [2] proposed a medical image encryption algorithm using the DNA–chaos cryptosystem. Suri et al. [18] proposed an image encryption approach based on coupled map lattice, DNA, and multiobjective genetic algorithm. Furthermore, with increasing demand for high-quality images, image compression techniques have become an effective way to save memory space and transmission bandwidth. As a result, some scholars have introduced image compression techniques to encryption systems, such as compressed sensing [6,19,20], self-encoder [12,21,22], cosine transform [20,23], and wavelet transform [3,24–27], etc.

In [2,8,9,13–18], several encryption schemes based on spatial domain are proposed. Image spatial domain encryption is fidelity encryption. In some spatial image encryption algorithms, the overly simple scrambling–diffusion schemes cannot effectively break the strong correlation of the plain image, making the algorithms vulnerable to chosen-plaintext attacks. Therefore, some researchers have designed multiround encryption structures to enhance the security level, which leads to inefficient encryption. However, for frequency domain encryption schemes, each change of coefficients in the transform domain leads to the change of all pixel values in the image spatial domain, and some scholars have shifted research directions to the more efficient frequency domain. Belazi et al. [24] proposed a novel image encryption scheme based on chaotic system and lifting wavelet transform. In [28], a new method of image encryption using fractional Fourier transform is proposed. With the emergence of encryption algorithms based on the spatial and frequency domains, hybrid domain encryption algorithms are proposed. Hybrid domain encryption, which combines the fidelity of spatial domain algorithms and the efficiency of frequency domain algorithms, provides high-level security. Aashiq et al. [3] proposed a medical image encryption method based on a chaos–DNA–IWT (integer wavelet transform) combined approach. However, the diffusion algorithm in this paper did not consider to employ bit-level diffusion, which has better diffusion performance. Luo et al. [25] proposed an encryption scheme using the IWT. In this paper, the authors used spatiotemporal chaos to diffuse low-frequency subbands and kept the high-frequency subbands unchanged. The diffusion algorithm did not take the full information of the image into account.

Based on the above analysis and to move beyond, we proposed a hybrid domain image encryption algorithm based on improved Henon map. The main contributions of this paper are summarized as follows:

(1) We improve the classical two-dimensional (2D) Henon map. The improved Henon map is briefly called 2D-ICHM. The analyses of dynamical properties show that 2D-ICHM has more complex chaotic behavior and is more suitable for image encryption scenarios.

(2) The proposed algorithm adopts a double sandwich structure based on diffusion–scrambling–diffusion and spatial domain–frequency domain–spatial domain. Specif-

ically, the diffusion and scrambling operations are performed in the spatial and frequency domains, respectively, which provides a high level of security.

(3) To enhance plaintext sensitivity, the system parameters and initial values of chaotic mapping are obtained by the secure hash algorithm-512 (SHA-512) hash value of the plain image and the given parameters. Therefore, the proposed algorithm is highly related to plain image.

The remainder of the paper is organized as follows. In Section 2, we introduce the research status of the chaotic system. In Section 3, the 2D-ICHM is proposed and the dynamic performance is analyzed. In Section 4, related knowledge is introduced. In Section 5, we describe the proposed image encryption algorithm in detail. In Section 6, the simulation results are given. In Section 7, security analyses are presented. Finally, the conclusion of this paper is reported in Section 8.

2. Chaotic System

Chaotic systems are often used to design image encryption algorithms, due to their numerous excellent intrinsic characteristics, including unpredictability, aperiodicity, and pseudorandom behaviors [29,30]. In the image encryption algorithm, chaotic sequences generated by chaotic systems are often used in the process of image scrambling and diffusion. Chaotic systems are categorized as one-dimensional (1D) and high-dimensional (HD) systems, which have been a hot research topic for scholars. The classical 1D chaotic systems have the logistic, sine, and tent maps [31]. Due to the low complexity and easy predictability of 1D chaotic maps, the chaotic sequences generated by such maps are less stochastic and cause a number of security risks in image encryption processing. The HD chaotic systems have larger parameter space and more complex structure than the 1D chaotic systems, making the behavior of chaotic sequences more difficult to predict and more suitable for image encryption theoretically. However, chaotic systems with too high dimensions are not suitable for designing real-time image encryption systems, as they lead to intensive calculations and high implementation costs. The 2D chaotic systems, with higher complexity and lower implementation cost, provide a balance of chaotic performance and implementation cost. Hence, our scheme chooses to use 2D chaotic systems.

The classical 2D chaotic systems include cat map, standard map, Henon map, etc. [32,33]. In recent years, some weak chaotic characteristics of the classical 2D chaotic systems have been pointed out, such as small parameter space, discontinuous chaotic intervals, and poor pseudorandomness. Thus, researchers have made some improvements or proposed new 2D chaotic systems [34–37]. Hua et al. [34] proposed a new two-dimensional sine logistic modulation map based on a logistic map and a sine map. Zhu et al. [35] constructed a new two-dimensional chaotic system by using logistic and sine maps. Bao et al. [36] proposed a novel two-dimensional sine map (2D-SM) with a simple algebraic structure. A color image encryption algorithm using the improved Henon map (IHM) was proposed by Gao [37]. Figure 1 shows the phase portraits and bifurcation diagrams of the classical 2D Henon map (2D-CHM), 2D-SM, and IHM. The phase portrait and bifurcation diagram are the most common indicators to identify chaotic states. The phase portrait can represent the reciprocating nonperiodic motion characteristics of chaotic systems. The bifurcation diagram can clearly reflect the period-doubling bifurcation phenomenon and parameter range of chaotic systems, etc. As shown in Figure 1a–c, the motion trajectories of 2D-CHM, 2D-SM, and IHM are not uniformly distributed, indicating they have weaker randomness. As shown in Figure 1d–f, the 2D-CHM, 2D-SM, and IHM have discontinuous chaotic intervals and a small range of parameters. Therefore, it is crucial to design a 2D chaotic system with better chaotic performance.

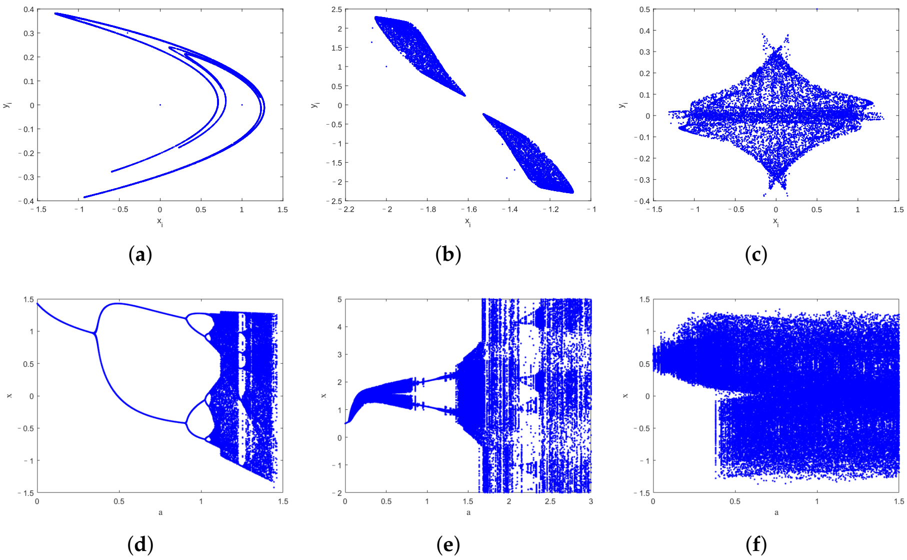

(**a**) (**b**) (**c**)

(**d**) (**e**) (**f**)

Figure 1. The phase portraits and bifurcation diagrams. Phase portraits: (**a**) 2D-CHM with $(a, b) = (1.4, 0.3)$, (**b**) 2D-SM with $(a, b) = (0.7, 3.8)$, (**c**) IHM with $(a, b) = (1, 0.3)$, $r = 0.1$; bifurcation diagrams: (**d**) the 2D-CHM with $b = 0.3$, (**e**) 2D-SM with $b = 3.8$, (f) IHM with $b = 0.3$, $r = 0.1$.

3. Improvement of the Classical Two-Dimensional Henon Map

In this section, we give the definition of the 2D-ICHM and analyze its dynamical behavior. Further, comparison of the dynamical behavior of 2D-ICHM, 2D-CHM, 2D-SM, and IHM is considered.

3.1. Definition of 2D-ICHM

Henon map [38], a simple 2D discrete chaotic system, was introduced by Henon in 1976, which is defined as

$$\begin{cases} x(n+1) = 1 + y(n) - ax(n)^2, \\ y(n+1) = bx(n), \end{cases} \tag{1}$$

where $(x(n), y(n)) \in R^2$ are the state values of system, $a \in [0, 1.4]$, and $b \in [0, 0.3]$ are control parameters.

When $a = 1.4$ and $b = 0.3$, the 2D-CHM has the maximum Lyapunov exponent (LE), showing a most significant chaotic behavior. However, the 2D-CHM has some disadvantages, such as simple chaotic behavior and discontinuous chaotic intervals. In order to overcome the above shortcomings, we improve the 2D-CHM to 2D-ICHM, defined as follows:

$$\begin{cases} x(n+1) = \cos(1 - ax(n)^2) + e^{by(n)^2}, \\ y(n+1) = \sin(x(n)^2), \end{cases} \tag{2}$$

where a and b are control parameters.

3.2. Chaotic Performance of 2D-ICHM

In order to verify the chaotic performance of the 2D-ICHM, the following analyses are discussed in terms of phase portrait, bifurcation diagram, Lyapunov exponent, approximate entropy, NIST SP800-22 test, and 0–1 test.

(1) Phase portrait and bifurcation diagram

Figure 2a is the phase portrait of 2D-ICHM with initial values $(x(0), y(0)) = (0.3, 0.3)$, and the control parameters $(a, b) = (5, 5)$. Figure 2b,c are the bifurcation diagrams of 2D-ICHM with $a \in (-50, 50)$, $b = 5$, and with $a = 5$, $b \in (0, 50)$, respectively.

As observed in Figures 1a–c and 2a, the attractor structures of the 2D-CHM, 2D-SM, IHM, and 2D-ICHM are different. The attractor of 2D-ICHM is a noiselike pattern. It indicates that 2D-ICHM has better ergodicity. As can be seen from Figures 1d–f and 2b,c, the bifurcation diagrams of the x and y components of the 2D-ICHM are also noiselike patterns, where the control parameters $a \in (-50, 50)$ and $b \in (0, 50)$. It indicates that 2D-ICHM has a larger parameter space and continuous chaotic range. Taken together, 2D-ICHM has a more complex chaotic behavior and is suitable for image encryption systems.

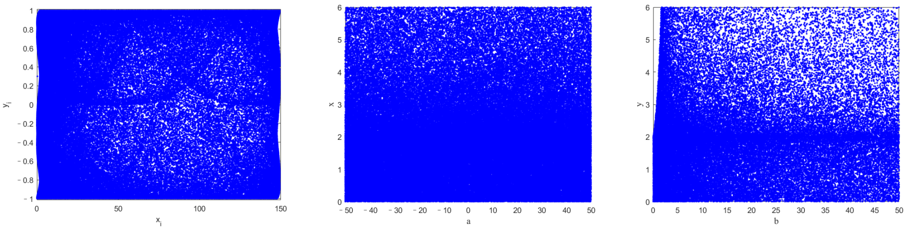

(**a**) (**b**) (**c**)

Figure 2. The phase portrait and bifurcation diagrams of the 2D-ICHM. (**a**) Phase portrait, (**b**) bifurcation diagram of output x, and (**c**) bifurcation diagram of output y.

(2) Lyapunov exponent

The LE can be used to evaluate the chaotic behavior of dynamical systems. It can reflect the average exponential rate of separation or aggregation between adjacent trajectories [39]. The number of LEs is equal to the dimension of the chaotic system, which means that 2D chaotic systems have two LEs. A map has chaotic behavior when there is one positive LE value. The chaotic behavior of the map becomes more complicated as its LE increases. LE can be calculated using the Qatari Rial (QR) decomposition algorithm [40], which is defined as follows.

$$\begin{aligned}
&= [J_M J_{M-1} \cdots J_2(J_1 Q_0)] \\
&= qr[J_M J_{M-1} \cdots J_3(J_2 Q_1)][R_1] \\
&= qr[J_M J_{M-1} \cdots J_i(J_{i-1} Q_{i-2})][R_{i-1} \cdots R_1] \\
&= \cdots \\
&= Q_M[R_M \cdots R_2 R_1] \\
&= Q_M R,
\end{aligned} \tag{3}$$

where $qr[\cdot]$ is the QR decomposition function, J is the Jacobian matrix of the chaotic map, and M is the number of iteration. Then, LE is calculated by

$$LE_v = \frac{1}{M} \sum_{i=1}^{M} \ln|R_i(v, v)|, \tag{4}$$

where $v = 1, 2, \cdots, n$.

The LEs of 2D-CHM, 2D-SM, IHM, and 2D-ICHM are calculated by QR decomposition algorithm, and Figure 3 plots their largest LEs. The figures are obtained by changing the parameter a when other parameters are fixed. A comparison on the largest LEs of the above four chaotic systems is given in Figure 3e. It is noted from this that 2D-ICHM has a larger and continuous positive LE value. Thus, 2D-ICHM has a more continuous chaotic range, which means it is suitable for image encryption systems.

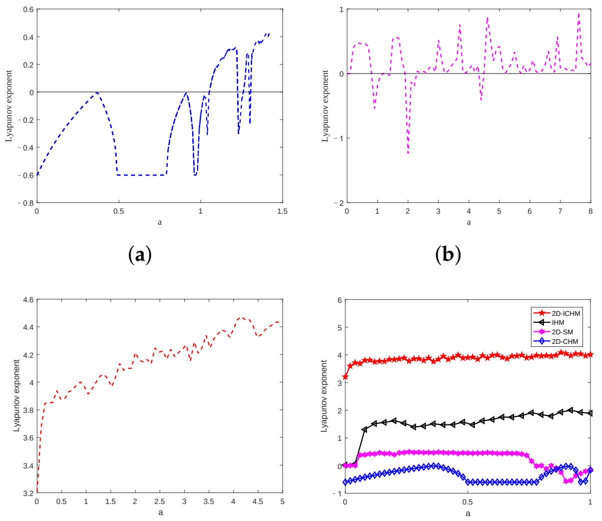

(**a**) (**b**) (**c**)

(**d**) (**e**)

Figure 3. The largest LE. (**a**) 2D-CHM with $b = 0.3$, (**b**) 2D-SM with $b = 3.8$, (**c**) IHM with $b = 0.3$ and $r = 0.1$, (**d**) 2D-ICHM with $b = 5$, (**e**) comparison of four maps.

(3) Approximate entropy

The complexity of nonlinear time series can be evaluated by the approximate entropy (ApEn), which increases with the increase of ApEn value. The calculation process of the ApEn is shown as follows [41]:

Step 1: Given a time series $x(1), x(2), \cdot\cdot\cdot, x(N)$, divide them into m-dimensional vectors

$$X(i) = [x(i), x(i+1), \cdots, x(i+m-1)], \tag{5}$$

where $i = 1, 2, 3, \cdots, N - m + 1$.

Step 2: Measure the distance between $X(i)$ and $X(j)$ by

$$d(i,j) = \max_{k=0,1,\cdots,m-1} [|x(i+k) - x(j+k)|], \tag{6}$$

where $i = 1, 2, 3, \cdots, N - m + 1$, $j = 1, 2, 3, \cdots, N - m + 1$.

Step 3: Set a threshold value $r (r > 0)$, define for each i, $1 \le i \le N - m + 1$,

$$C_i^m(r) = (\text{number of } j \text{ such that } d(i,j) < r)/N - m + 1, \tag{7}$$

where $j = 1, 2, 3, \cdots, N - m + 1$.

Step 4: Denote the mean of logarithm of $C_i^m(r)$ as $\varphi^m(r)$ and we have

$$\varphi^m(r) = \frac{1}{N-m+1} \sum_{i=1}^{N-m+1} \ln C_i^m(r). \tag{8}$$

Step 5: Change the dimension m to $m + 1$ and repeating step 1 to step 4, the ApEn is

$$ApEn(m,r) = \lim_{N \to \infty} \left[\varphi^m(r) - \varphi^{m+1}(r) \right]. \tag{9}$$

In practical terms, the length of the data sequence is bounded. Therefore, the ApEn algorithm is changed into

$$ApEn(m,r,N) = \varphi^m(r) - \varphi^{m+1}(r). \tag{10}$$

In order to keep the correlation between ApEn and N to a minimum, Pincus found that parameters can be set to $m = 2$ and $r \in [0.1SD(x), 0.2SD(x)]$, $SD(x)$ is the standard deviation of x [42]. Using the above algorithm, the ApEn values of the 2D-CHM, 2D-SM, IHM, and 2D-ICHM are shown in Figure 4. As shown in Figure 4, 2D-ICHM has a higher ApEn value; therefore, the output time series of 2D-ICHM has higher complexity.

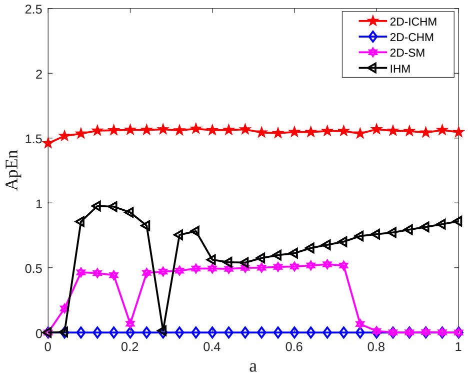

Figure 4. The ApEn comparison among the 2D-ICHM ($b = 5$), 2D-CHM ($b = 0.3$), 2D-SM ($b = 3.8$, $r = 0.1$), and IHM ($b = 0.3$).

(4) NIST SP800-22 test

The level of security of an image encryption system depends heavily on the randomness of the pseudorandom number sequence. NIST SP800-22 test [43] can be used to evaluate the random characteristics of binary bit sequences. The NIST SP800-22 test provides 15 test methods, including frequency test, run test, approximate entropy test, random excursions test, etc. Each test calculates a random value to determine whether the binary sequence is random. If $p\_value > 0.01$, the binary sequence is considered to be random, and the larger the p_value, the better the randomness. The SP800-22 test recommends that the length of the binary sequence tested is from 10^3 to 10^7. Therefore, the test binary sequence we used is 10^6 in length. As we can see from Table 1, all the calculated p_value are larger than 0.01. Therefore, the 2D-ICHM has passed all the random tests, which shows that the 2D-ICHM is more suitable for image encryption.

Table 1. SP800-22 test.

Statistical Test	***p_Value***
Frequency	0.9856
Block Frequency	0.8178
Cumulative Sums	0.2113
Runs	0.1421
Longest Run	0.6101
Rank	0.3482
Fft	0.5341
Nonoverlapping Template	0.9114
Overlapping Template	0.5341
Approximate Entropy	0.3504
Random Excursions	0.6528
Frequency	0.8562
Random Excursions Variant	0.7236
Serial	0.7399
Linear Complexity	0.0179

(5) 0–1 test

G. A. Gottwald and I. Melbourne proposed a reliable and effective binary test method for checking whether the dynamical system is chaos, which is called the “0–1 test” [44]. It can be described as

Step 1: For a time series $x(j)(j=1,2,\cdots,N)$, the definition of translation variables is

$$\begin{cases} p_c(n)=\sum\limits_{j=1}^{n} x(j)\cos(jc), \\ q_c(n)=\sum\limits_{j=1}^{n} x(j)\sin(jc), \end{cases} \tag{11}$$

where $c \in (0,\pi)$ and $n=1,2,\cdots,N$.

Step 2: In order to measure the diffusive (or nondiffusive) behavior of p_c and q_c, the mean square displacement defined as

$$M_c(n)=\lim_{N\to\infty}\frac{1}{N}\sum_{j=1}^{N}\left\{[p_c(j+n)-p_c(j)]^2+[q_c(j+n)-q_c(j)]^2\right\}, \tag{12}$$

where $n \leq N_0 << N$. In practice, $N_0 = round(N/10)$.

Step 3: Define the modified mean square displacement $D_c(n)$ as

$$D_c(n)=M_c(n)-V_{osc}(c,n), \tag{13}$$

where $V_{osc}(c,n)=\left[\lim\limits_{N\to\infty}\frac{1}{N}\sum\limits_{j=1}^{N}x(j)\right]^2\frac{1-\cos(nc)}{1-\cos(c)}$.

Step 4: Define the vectors and the correlation coefficient

$$\begin{cases} \Delta=(D_c(1),D_c(2),\cdots,D_c(N_0)), \\ K_c=corr(\xi,\Delta)\in[-1,1], \end{cases} \tag{14}$$

where $\xi=1,2,\cdots,N_0$. $K_c \approx 0$ indicates regular behaviour, while $K_c \approx 1$ indicates chaotic behaviour.

Figure 5 shows the 0–1 test results of 2D-ICHM with $c=2$, and initial values $(x(0),y(0))=(0.3,0.3)$. As shown in Figure 5a, K_c is very close to 1, illustrating that the 2D-ICHM has significant chaotic behavior. In addition, The (p,q) plane also can intuitively reflect whether the dynamic system is chaotic or not. When the trajectory of the (p,q) plane is bounded motion, the dynamical system is regular, and when the trajectory of the (p,q) plane is Brownian-like motion, the dynamical system is chaotic. The (p,q) planes of the 2D-ICHM are shown in Figure 5b,c. It can be seen that the trajectories of 2D-ICHM are similar to Brownian motion. This means that the 2D-ICHM is a chaotic dynamic system.

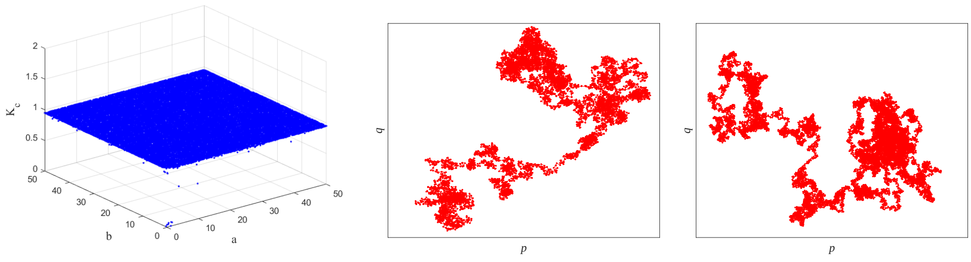

(**a**) (**b**) (**c**)

Figure 5. 0–1 test results. (**a**) Plot of K_c versus a and b, (**b**) (p,q) plane of the x sequence with $(a,b)=(5,5)$, (**c**) (p,q) plane of the y sequence with $(a,b)=(5,5)$.

4. Relevant Knowledge

4.1. Bit-Plane Decomposition

The recombined plane of binary pixel values at the same bit positions of a grayscale image is called the bit plane. The grayscale image $P = \{p(i,j)\}$ is decomposed into eight binary bit planes $P_k = \{p_k(i,j)\}(k = 1, 2, \cdots, 8)$ [45], given by

$$P = \sum_{k=1}^{8} P_k 2^{k-1} = P_1 2^0 + P_2 2^1 + \cdots + P_8 2^7. \tag{15}$$

Figure 6a is a grayscale image "Lena" of size 256 × 256. The eight binary planes of "Lena" are shown in Figure 7a–h. The higher bit plane contains more information, among which the high four bit planes contain more than 94% of information in the original image [46]. A composite image of high four bit planes is shown in Figure 6b, which retains the vast majority of the original image.

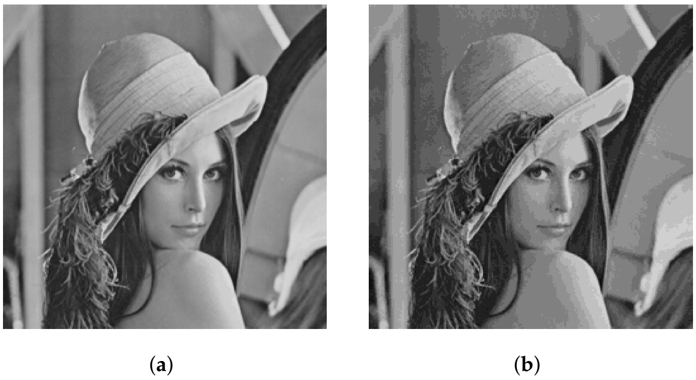

Figure 6. Lena and composite image of high four bit planes. (**a**) Lena, (**b**) composite image of high four bit planes.

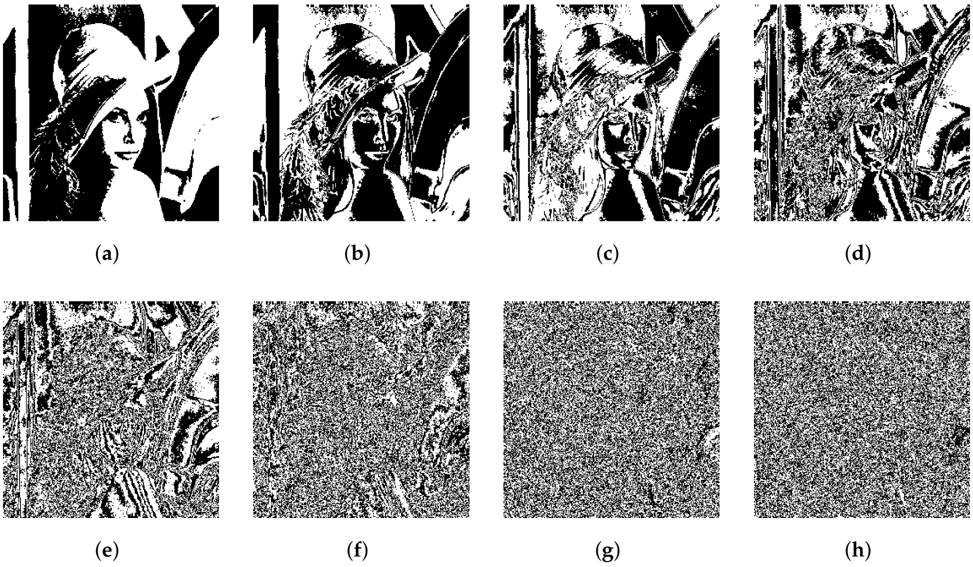

Figure 7. The corresponding eight bit planes of Lena. (**a**) P_8, (**b**) P_7, (**c**) P_6, (**d**) P_5, (**e**) P_4, (**f**) P_3, (**g**) P_2, and (**h**) P_1.

4.2. Integer Wavelet Transform

Wavelet transform links the time domain and frequency domain of the image. The IWT was proposed by Swelden and Daubechies in 1998 [47]. Compared with the traditional wavelet transform, the IWT has obvious advantages, e.g., low computational complexity, no edge effect, and complete reversibility. The image can be decomposed into four bands

LL, LH, HL, and HH using IWT (see Figure 8). Most of the detailed information in the image is concentrated in the low frequency band LL [48].

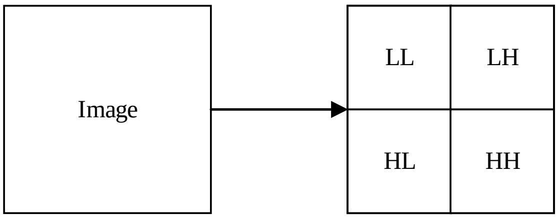

Figure 8. IWT operations.

4.3. DNA Sequence Operations

DNA sequence operations consist of two components: DNA encoding/decoding and DNA computation.

(1) DNA encoding and decoding rules

The DNA sequence of biology contains four nucleic acid bases i.e., A (Adenine), C (Cytosine), G (Guanine), and T (Thymine), where A and T, G, and C are complementary, respectively [49]. In binary computing, 0 and 1 are complementary, so the binary digits 00 and 11 are complementary, as well as 01 and 10. The binary digits 00, 01, 10, and 11 can be encoded as the four bases A, T, C, and G. There are 24 kinds of coding rules, while only eight coding rules are capable of meeting the Watson-Crick complement rule, as listed in Table 2. A pixel value denoted by eight bits can be encoded as a DNA sequence containing four bases. For example, a decimal pixel value is 150, and its corresponding binary is [10010110]. Different coding rules yield different combinations of bases. If we use Rule 3, [10010110] is encoded as [TAAT]. Decoding is the inverse process of encoding. The inverse of Rule 3 can be used to decode [TAAT] into [10010110].

Table 2. DNA coding rules.

Rules	**1**	**2**	**3**	**4**	**5**	**6**	**7**	**8**
00	A	A	C	C	G	G	T	T
01	C	G	A	T	A	T	C	G
10	G	C	T	A	T	A	G	C
11	T	T	G	G	G	G	A	A

(2) DNA computation

The computation of DNA sequences includes DNA addition, subtraction, and XOR operations, where DNA addition and DNA subtraction operations are reciprocal. These three DNA computations are all used in this paper. The eight different DNA coding rules in Table 2 correspond to eight different DNA addition, subtraction and XOR operations. In this paper, we use the coding Rule 4, whose corresponding DNA addition and XOR operations are shown in Table 3.

Table 3. DNA addition operations and XOR operations.

+	**A**	**C**	**G**	**T**	**XOR**	**A**	**C**	**G**	**T**
A	C	A	T	G	A	C	A	T	G
C	A	C	G	T	C	A	C	G	T
G	T	G	A	C	G	T	G	C	A
T	G	T	C	A	T	G	T	A	C

5. The Proposed Image Encryption Algorithm

5.1. Generating Chaotic Sequences

In order to enhance the correlation of the proposed algorithm and the plain image. the system parameters and initial values of the 2D-ICHM are generated by the SHA-512 hash values of the plain image. The process of generating chaotic sequences is specified as follows.

Step 1: The SHA-512 hash values of the plain image are divided into 64 8-bit blocks: $K = [k_1, k_2, \cdots, k_{64}]$. The parameters $s_1, s_2, s_3, s_4, s_5, s_6$ can be calculated by

$$\begin{cases} s_1 = \frac{k_1+k_2+\cdots+k_8}{8\times 2^8}, \\ s_2 = \frac{k_9\oplus k_{10}\oplus\cdots\oplus k_{16}}{2^8}, \\ s_3 = \frac{k_{17}\oplus k_{18}\oplus\cdots\oplus k_{24}}{2^8}, \\ s_4 = \frac{k_{25}\oplus k_{26}\oplus\cdots\oplus k_{32}}{2^8}, \\ s_5 = \frac{(k_{33}+k_{34})\oplus(k_{35}+k_{36})\oplus\cdots\oplus(k_{47}+k_{48})}{2\times 2^8}, \\ s_6 = \frac{(k_{49}\oplus k_{50})+(k_{51}\oplus k_{52})+\cdots+(k_{63}\oplus k_{64})}{8\times 2^8}, \end{cases} \tag{16}$$

where $x \oplus y$ is the bitwise XOR operator. The system parameters a_0, b_0 and initial values x_0, y_0 of 2D-ICHM are calculated as follows.

$$\begin{cases} a_0 = \bmod\left((s_1 + s_2 + s_3) \times 10^8, 256\right)\Big/255 + v_1, \\ b_0 = \bmod\left((s_2 + s_3 + s_4) \times 10^8, 256\right)\Big/255 + v_2, \\ x_0 = \bmod\left((s_3 + s_4 + s_5) \times 10^8, 256\right)\Big/255 + v_3, \\ y_0 = \bmod\left((s_4 + s_5 + s_6) \times 10^8, 256\right)\Big/255 + v_4, \end{cases} \tag{17}$$

where v_1, v_2, v_3, v_4 are real numbers. The K, v_1, v_2, v_3 and v_4 are secret keys.

Step 2: To eliminate the transient effect and improve security of the system, 2D-ICHM is performed with N_0 pre-iterations. Then it is iterated $M \times N$ times, where M and N represent the width and height of the plain image, respectively. We use i to represent the index of the number of iterations. After each iteration, state values $X(i), Y(i)$ are stored in the sequence X, Y, respectively.

Step 3: The two chaotic sequences X^1, Y^1 are calculated by

$$\begin{cases} X^1(i) = \bmod\left(\lfloor(|X(i)| - \lfloor|X(i)|\rfloor) \times 2^{16}\rfloor, 256\right), \\ Y^1(i) = \bmod\left(\lfloor(|Y(i)| - \lfloor|Y(i)|\rfloor) \times 2^{16}\rfloor, 256\right), \end{cases} \tag{18}$$

where $\lfloor\cdot\rfloor$ denotes the round-down operation, and $i = 1, 2, \cdots, M \times N$.

5.2. Encryption Process

The encryption process is as follows. The process of high bit planes diffusion in the space domain corresponds to Steps 2–3, the process of scrambling operation in the frequency domain corresponds to Steps 4–7, and the process of DNA computing and bidirectional diffusion in the spatial domain corresponds to Steps 8–10.

Step 1: The plain image P of size $M \times N$ is decomposed into eight binary bit planes $P_1, P_2, \cdots, P_8$.

Step 2: Arrange the high bit planes P_i $(i = 5, 6, 7, 8)$ into binary vectors P_i' $(i = 5, 6, 7, 8)$ from top to down row by row. Take the first $MN/8$ terms of the chaotic sequence X^1 and convert it into the binary sequence H_1.

Step 3: The new binary vectors $P''_i (i = 5, 6, 7, 8)$ are generated by the diffusion operation of Equation (19). The vectors $P''_i (i = 5, 6, 7, 8)$ are transformed into the bit planes $\hat{P}_i$ $(i = 5, 6, 7, 8)$ according to the top to down and left to right rules.

$$\begin{cases} P''_8 = bitxor(P'_8, H_1), \\ P''_7 = bitxor(P'_7, \hat{P}_8), \\ P''_6 = bitxor(P'_6, \hat{P}_7), \\ P''_5 = bitxor(P'_5, \hat{P}_6), \end{cases} \tag{19}$$

where $bitxor(x, y)$ represents bit by bit XOR operations. The intermediate cipher image Q_1 is obtained using Equation (20).

$$Q_1 = P_1 2^0 + P_2 2^1 + P_3 2^2 + P_4 2^3 + \hat{P}_5 2^4 + \hat{P}_6 2^5 + \hat{P}_7 2^6 + \hat{P}_8 2^7. \tag{20}$$

Step 4: The IWT is applied to Q_1 to obtain the bands LL, LH, HL and HH of each size $M/2 \times N/2$. To visualize the Chunking-Arrangement-Combination operation, an example is provided in Figure 9 $(M = 12, N = 12)$.

Step 5: LL is divided into 4 sub-blocks of size $m \times n$ (see Figure 9b, $m = 3, n = 3$). Convert each sub-block to a vector of length $m \times n$ by arranging the first column sub-blocks from left to right row by row and the second column sub-blocks from top to down column by column (see Figure 9c). After that, sub-vectors are recombined into a vector Z_1 of length $4 \times m \times n$ according to the combination method of Figure 9d.

Step 6: Using the method in Step 5 to convert LH, HL and HH to vectors Z_2, Z_3 and Z_4, respectively. Take the first $MN/4$ terms of the chaotic sequence X^1 to obtain the sequence X^2. By arranging the sequence X^2 in ascending order, the index sequence I is obtained.

Step 7: The vectors Z^1, Z^2, Z^3 and Z^4 are obtained by using the global scrambling operation of Equation (21).

$$Z^i(j) = Z_i(I(j)), \tag{21}$$

where $i = 1, 2, 3, 4$ and $j = 1, 2, \cdots, M \times N/4$. Then Z^1, Z^2, Z^3 and Z^4 are transformed into matrices LL^1, LH^1, HL^1 and HH^1 according to the top to down and left to right rules. The intermediate cipher Q_2 is obtained by applying inverse IWT of LL^1, LH^1, HL^1 and HH^1.

Step 8: Arrange Q_2 into binary vectors Q'_2 from top to down row by row, and convert chaotic sequence Y^1 into binary sequence H_2. Convert Q'_2, H_1, H_2 into DNA sequences $\hat{Q}'_2, H_1^1, H_2^1$ by DNA coding Rule 4 in Table 2. Then the DNA addition and XOR operations (see Table 3) are performed on the above DNA sequences using Equation (22) to obtain the sequence H_3.

$$H_3 = DNA\_xor(DNA\_add(\hat{Q}'_2, H_1^1), H_2^1). \tag{22}$$

Step 9: The inverse of DNA coding Rule 3 is used to decode H_3 to obtain the binary sequence Q'_3.

Step 10: Q'_3 is converted to the decimal sequence Q_3. Then we use the bidirectional diffusion processing of Equation (23) to obtain the sequence Q_4.

$$\begin{cases} E(i) = E(i-1) \times X^1(i) \times Q_3(i), \\ Q_4(j) = Q_4(j+1) \times Y^1(j) \times E(j), \end{cases} \tag{23}$$

where $i = 1, 2, \cdots, MN$, $j = MN - 1, MN - 2, \cdots, 1$, "×" denotes GF(257) field multiplication, $E(0)$ and $Q_4(0)$ are positive integers and take values in the range 0 to 255, $Q_4(MN) = Q_4(0) \times Y^1(MN) \times E(MN)$. $E(0)$ and $Q_4(0)$ are secret keys.

Step 11: The Q_4 is transformed into the final encrypted image C according to the top to down and left to right rules.

The encryption flow chart of the proposed algorithm is shown in Figure 10. Decryption can be completed by performing the reverse operation of encryption. The decryption flow chart is shown in Figure 11.

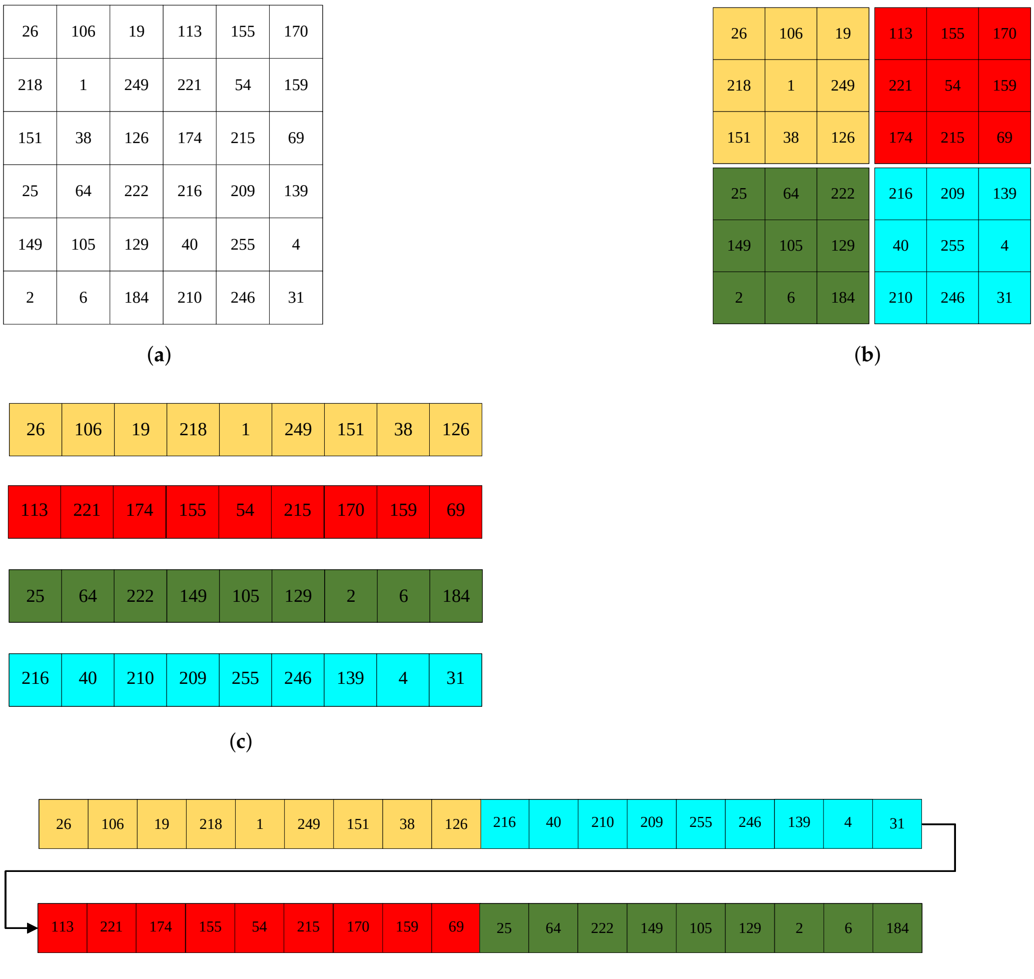

26	106	19	113	155	170
218	1	249	221	54	159
151	38	126	174	215	69
25	64	222	216	209	139
149	105	129	40	255	4
2	6	184	210	246	31

(**a**)

26	106	19	113	155	170
218	1	249	221	54	159
151	38	126	174	215	69
25	64	222	216	209	139
149	105	129	40	255	4
2	6	184	210	246	31

(**b**)

26	106	19	218	1	249	151	38	126
113	221	174	155	54	215	170	159	69
25	64	222	149	105	129	2	6	184
216	40	210	209	255	246	139	4	31

(**c**)

26	106	19	218	1	249	151	38	126	216	40	210	209	255	246	139	4	31
113	221	174	155	54	215	170	159	69	25	64	222	149	105	129	2	6	184

(**d**)

Figure 9. Example of Chunking—Arrangement—Combination. (**a**) 6 × 6 matrix, (**b**) chunking operations, (**c**) arrangements of sub-blocks, and (**d**) combination of vectors.

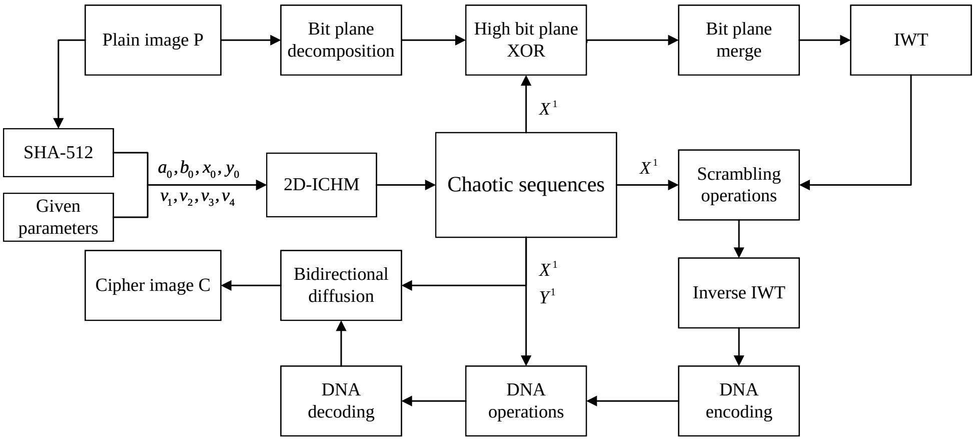

Figure 10. Encryption flow chart.

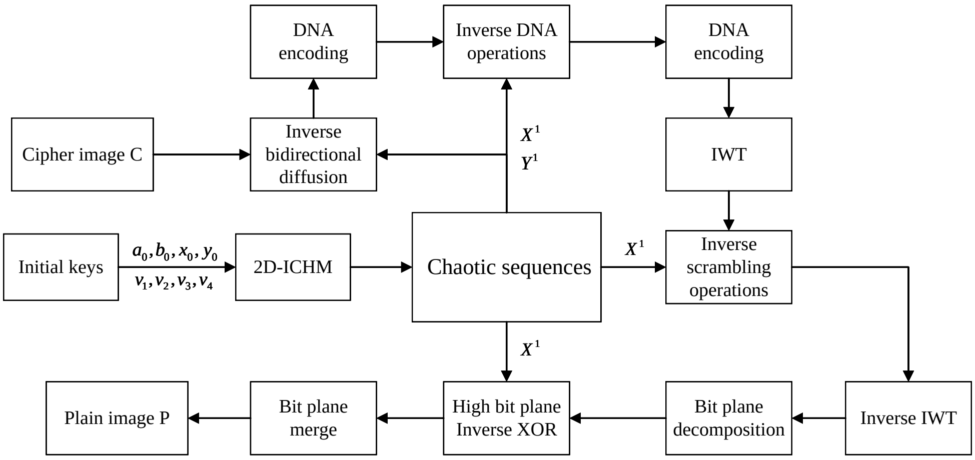

Figure 11. Decryption flow chart.

6. Simulation Results

The experimental environment is Intel(R) Core(TM) i5-9300HF CPU processor operating at 2.4 GHz, 8 GB of RAM, and a Microsoft Windows 10 operation system. We use Matlab 2016b to execute encryption and decryption programs. The experimental images are chosen from the CVG-UGR and USC-SIPI image databases. The parameters used in this paper are as follows: $v_1 = 80$, $v_2 = 20$, $v_3 = 2, v_4 = 2$, $E(0) = 20$, $Q_4(0) = 20$, and the size of sub-blocks $m \times n = 64 \times 64$. Four different 256×256 grayscale images "Lena", "Peppers", "5.1.10", and "5.1.11" are used as plain images.

The results of encryption and decryption are displayed in Figure 12. As can be seen, the cipher images are noise-like. It means that we cannot get useful information about the plain images from the cipher images. Furthermore, the decrypted images are identical to the plain images in visual respects. Thus, the proposed image encryption algorithm has excellent encryption and decryption effects.

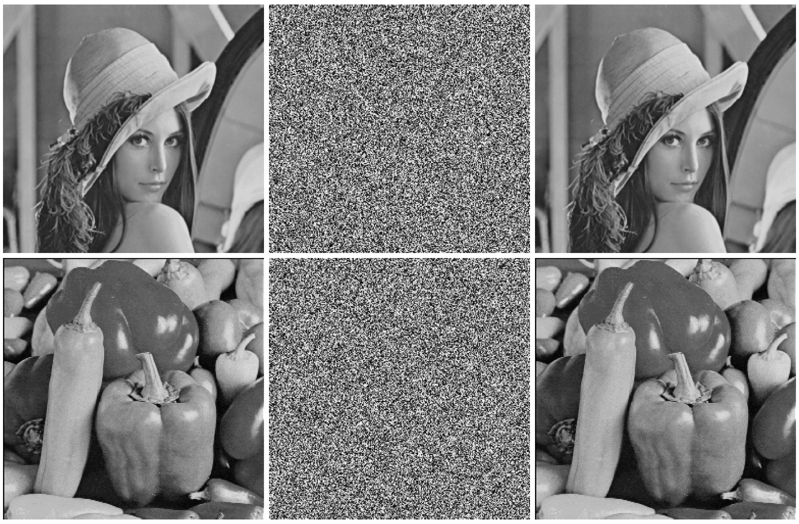

Figure 12. *Cont.*

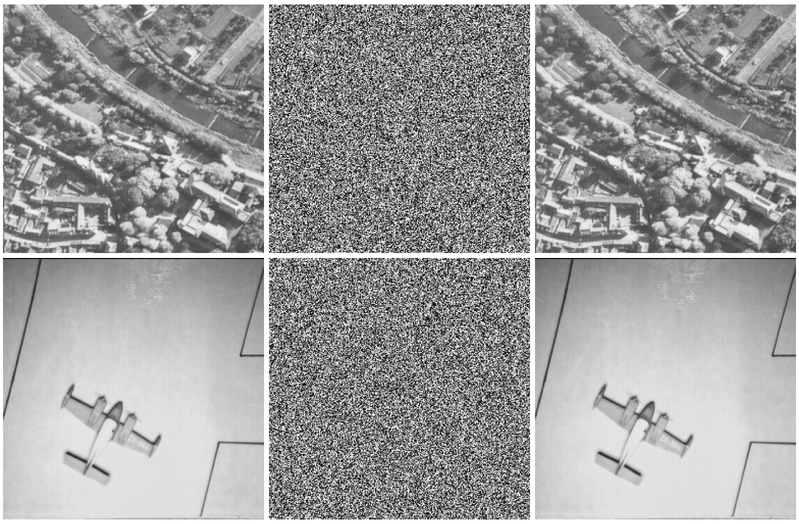

Figure 12. The simulation results of the proposed image encryption algorithm. The first column: plain images; the second column: encrypted images; the third column: decrypted images.

7. Security Analysis

In this section, we evaluate the security performance of the proposed algorithm through the analysis of key space, key sensitivity, histogram, correlation, information entropy, differential attack, chosen/known-plaintext attack, cropping attack, and noise attack.

7.1. Key Space Analysis

To counter brute force attacks, we should expand the key space of the algorithm as much as possible. The literature [50] stated that the key space of a secure encryption algorithm should be larger than 2^{100}. The secret key of the proposed algorithm includes three subkeys: (1) 512-bit hash value K of the plain image; (2) the given parameters v_1, v_2, v_3, and v_4; (3) the positive integers $E(0)$ and $Q_4(0)$. Suppose the operational precision of the computer is 10^{-14}; the key space of the proposed algorithm is $2^{512} \times 10^{14\times 4} \times 256 \times 256 > 2^{714}$, which is much larger than 2^{100}. The results compared with other algorithms are listed in Table 4. From Table 4, it is obvious that our key space is larger, which means that the proposed algorithm is resistant to brute force attacks.

Table 4. Key space for different algorithms.

Algorithms	Proposed	Ref. [6]	Ref. [16]	Ref. [51]	Ref. [52]	Ref. [53]	Ref. [54]
Key spaces	2^{714}	2^{99}	2^{598}	2^{213}	2^{186}	2^{496}	2^{512}

7.2. Key Sensitivity Analysis

A secure image encryption system should show a high sensitivity to the key. The key sensitivity can be considered in two aspects.

In the encryption process, using two keys with a tiny difference to encrypt the same plain image, the two encrypted images should be completely different. Take "Lena" as test image. The key sensitivity analysis results of the encryption process are shown in Figure 13, where K_1 is obtained by changing the 1st bit of K from 1 to 0. The cipher images C_1, C_2, and C_3 (Figure 13c–e) are obtained by using slightly different keys (A subkey is changed while the other subkeys remain unchanged). The subtraction images S_1, S_2, and S_3 (Figure 13f–h) with noiselike textures indicate that C_1, C_2, and C_3 are totally different from C.

In the decryption process, the plain image can only be decrypted correctly when the correct secret key is used. The key sensitivity analysis results of the decryption process are shown in Figure 14. It can be seen that when the decryption keys with a tiny difference are used, the decrypted images become noise images. The decrypted images are totally different from the correct plain images.

To quantitatively evaluate the key sensitivity of the proposed algorithm, the number of pixels change rate (NPCR) and unified average changing intensity (UACI) are adopted. For two random 8-bit noise images, the ideal values of NPCR and UACI are 99.61% and 33.46% [55]. The formula is defined as follows.

$$\begin{cases} NPCR = \frac{\sum_{i=1}^{M}\sum_{j=1}^{N} D(i,j)}{M \times N} \times 100\%, \\ UACI = \frac{\sum_{i=1}^{M}\sum_{j=1}^{N} |C_1(i,j) - C_2(i,j)|}{M \times N \times 255} \times 100\%, \end{cases} \tag{24}$$

where

$$D(i,j) = \begin{cases} 1, C_1(i,j) \neq C_2(i,j), \\ 0, C_1(i,j) = C_2(i,j), \end{cases} \tag{25}$$

C_1, C_2 represents two different cipher images, $M \times N$ represents the size of image.

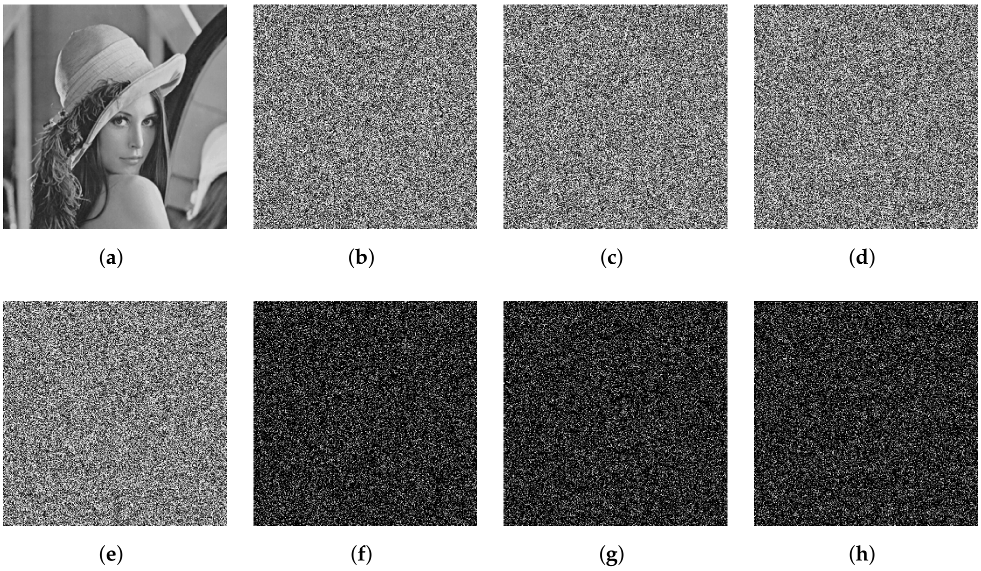

Figure 13. The key sensitivity analysis results of the encryption process. (**a**) Plain image "Lena", (**b**) cipher image C with correct keys, (**c**) cipher image C_1 with K_1, (**d**) cipher image C_2 with $v_1' = v_1 + 10^{-14}$, (**e**) cipher image C_3 with $v_3' = v_3 - 10^{-14}$, (**f**) subtraction image $S_1 = |C_1 - C|$, (**g**) subtraction image $S_2 = |C_2 - C|$, and (**h**) subtraction image $S_3 = |C_3 - C|$.

The calculated values of NPCR and UACI between the cipher image C (Figure 13b) and the cipher images C, C_1, C_2, and C_3 (Figure 13b–e) are listed in Table 5. It can be seen that the values of NPCR and UACI are close to the ideal values. This means that when slightly different keys are used in the encryption process, the cipher images obtained are totally different. Between a random noise image and a determinate Lena image, the ideal value of NPCR is 99.61% and the ideal value of UACI is 28.62% [56]. The calculated values of NPCR and UACI between the decrypted image D (Figure 14a) and the decrypted images D, D_1, D_2, and D_3 (Figure 14a–d) are listed in Table 6. It is clear that the values of NPCR and UACI are close to the ideal values. This means that when slightly different decryption keys are used in the decryption process, the decrypted images obtained are totally different. Therefore, the proposed encryption algorithm has a high sensitivity to the secret key.

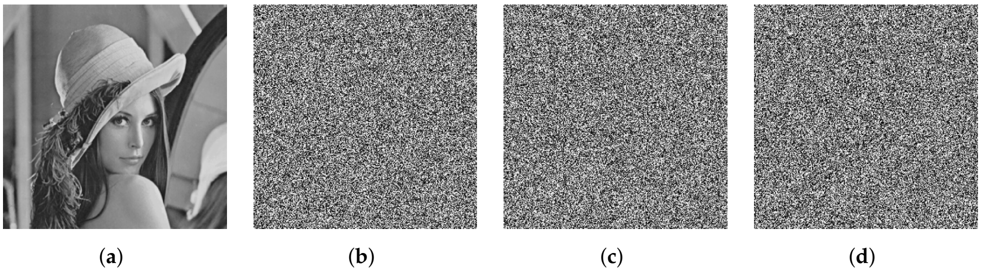

Figure 14. The key sensitivity analysis results of the decryption process. (**a**) Decrypted image D with correct keys, (**b**) decrypted image D_1 with K_1, (**c**) decrypted image D_2 with $v_1' = v_1 + 10^{-14}$, and (**d**) decrypted image D_3 with $v_3' = v_3 - 10^{-14}$.

Table 5. Values of NPCR and UACI of Lena's cipher images.

Secret Keys			**Calculated Values**	
			NPCR%	**UACI%**
v_1	v_3	K	0	0
v_1	v_3	K_1	99.61	33.55
$v_1' = v_1 + 10^{-14}$	v_3	K	99.60	33.45
v_1	$v_3' = v_3 - 10^{-14}$	K	99.62	33.46
	Ideal value		99.61	33.46

Table 6. Values of NPCR and UACI of Lena's decrypted images.

Secret Keys			**Calculated Values**	
			NPCR%	**UACI%**
v_1	v_3	K	0	0
v_1	v_3	K_1	99.62	28.65
$v_1' = v_1 + 10^{-14}$	v_3	K	99.65	28.57
v_1	$v_3' = v_3 - 10^{-14}$	K	99.58	28.60
	Ideal value		99.61	28.62

7.3. Histogram Analysis

The distribution of image pixel values can be reflected by the image histogram. If the histogram of a cipher image is flat, information of the plain image is excellently hidden. Figure 15 shows the histograms of the images before and after encryption. It can be seen that the histograms of encrypted images become relatively flat. Therefore, the proposed algorithm can effectively resist statistical attacks.

The chi-square test can be used to quantitatively analyze the uniformity of the histogram, which is defined by Equation (26).

$$\chi^2 = \sum_{i=0}^{255} \frac{(f_i - g)}{g}, \tag{26}$$

where $g = M \times N/256$, and f_i is the occurrence frequency of the pixels whose value is i. Given a significant level $\alpha = 0.05$, if $\chi^2_{0.05} < 293.2478$, the chi-square test is passed [57]. Table 7 shows that the calculated chi-square values for all cipher images are less than 293.2478. Therefore, all the cipher images encrypted by the proposed algorithm have passed the chi-square test, which means that the proposed algorithm can resist statistical attacks.

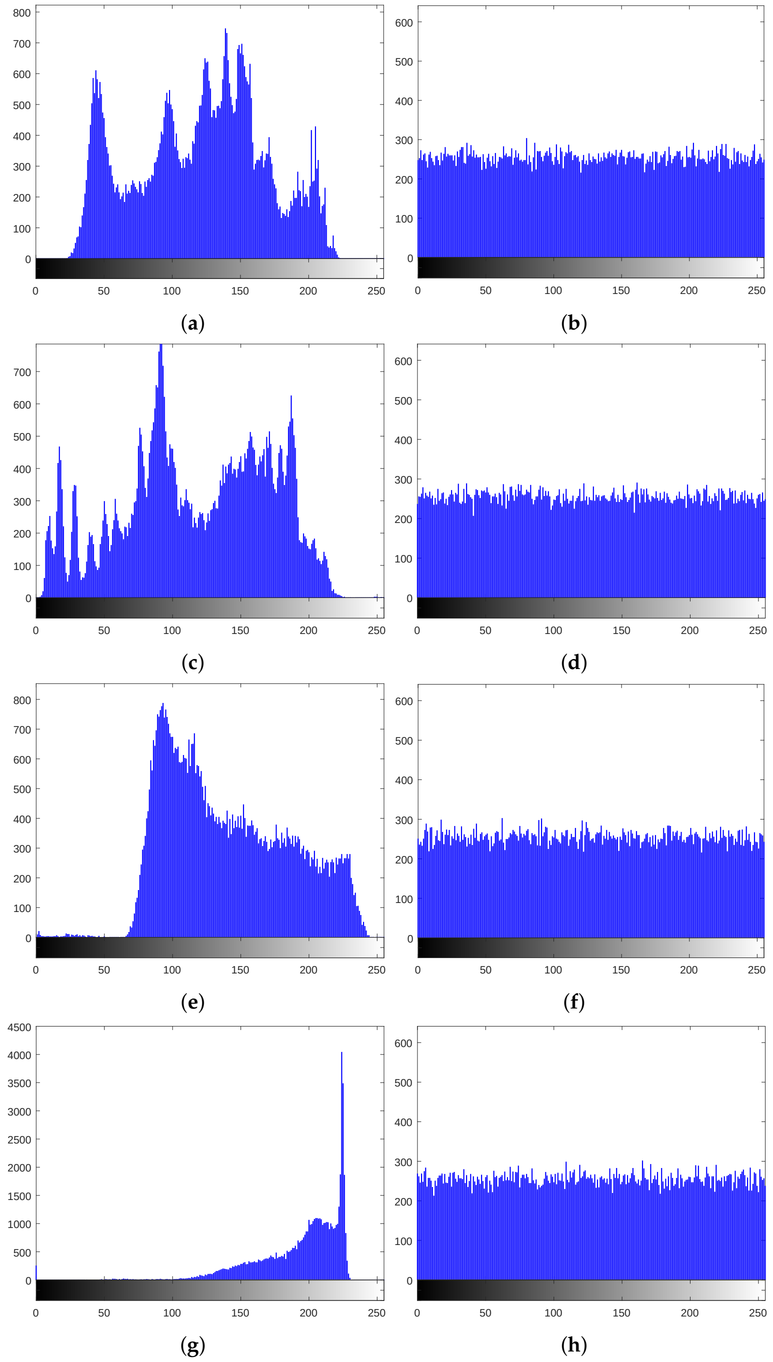

(**a**) (**b**) (**c**) (**d**) (**e**) (**f**) (**g**) (**h**)

Figure 15. Histogram results. Plain image: (**a**) Lena, (**c**) Peppers, (**e**) 5.1.10, and (**g**) 5.1.11; cipher image: (**b**) Lena, (**d**) Peppers , (**f**) 5.1.10, and (**h**) 5.1.11.

Table 7. χ^2 test.

Image	**Plain**	**Cipher**
Lena	4.2698×10^4	231.1174
Peppers	1.2892×10^5	271.2109
4.1.01	3.0295×10^5	271.6172
4.1.02	7.1297×10^5	258.7578
4.1.03	1.4396×10^6	230.5156
5.1.09	1.3569×10^5	219.5625
5.1.10	5.0863×10^4	240.9844

Table 7. *Cont.*

Image	Plain	Cipher
5.1.11	2.2085×10^5	258.7188
5.1.12	2.8206×10^5	275.6250
5.1.13	1.1983×10^7	239.3359
5.1.14	5.0326×10^4	251.0156
6.1.01	1.2230×10^5	225.1953

7.4. Correlation Analysis of Adjacent Pixels

The plain image with effective information has a strong correlation between adjacent pixels. The ideal encryption algorithm can eliminate the correlation of adjacent pixels to resist statistical attacks. To ensure the reliability of the experiment, 20,000 pairs of pixels are randomly selected to test the correlation in horizontal, vertical, and diagonal directions. As shown from Figure 16, the adjacent pixel distribution of the plain image is relatively concentrated, whereas the adjacent pixel distribution of the cipher image is noiselike. This means that the correlation of the plain image is greatly reduced. To quantitatively describe the correlation, the correlation coefficient is calculated as follows.

$$\begin{cases} E(x) = \frac{1}{N}\sum\limits_{i=1}^{N} x_i, \\ cov(x,y) = \frac{1}{N}\sum\limits_{i=1}^{N}(x_i - E(x))(y_i - E(y)), \\ D(x) = \frac{1}{N}\sum\limits_{i=1}^{N}(x_i - E(x))^2, \\ r_{xy} = \frac{cov(x,y)}{\sqrt{D(x)}\sqrt{D(y)}}. \end{cases} \tag{27}$$

The calculated correlation coefficients are shown in Table 8. It can be seen that the correlation coefficients of the cipher images have been greatly reduced, close to 0. The results compared with other algorithms as shown in Table 9. As can be seen, the correlation coefficients of Lena for the proposed algorithm are smaller in all three directions compared with [6,54], and the proposed algorithm has great advantages in the horizontal and diagonal directions compared with [16,51,52], and the proposed algorithm has certain advantages in the horizontal direction compared with [53]. The above results show that the proposed algorithm can effectively remove the correlation of adjacent pixels, so it provides a high level of security to resist statistical attacks.

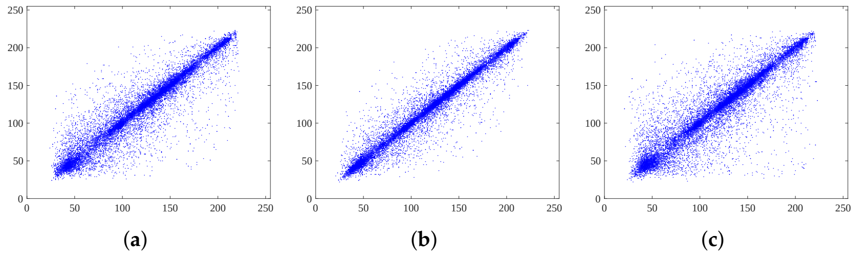

(**a**) (**b**) (**c**)

Figure 16. *Cont.*

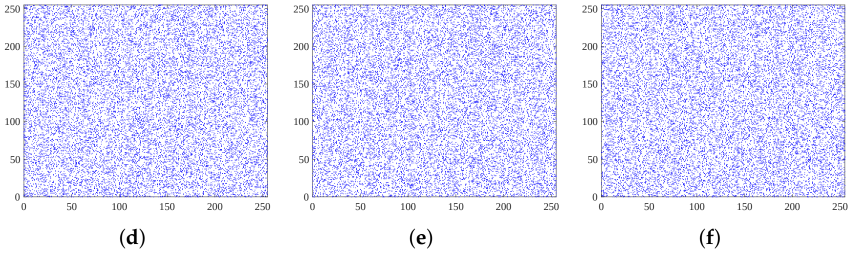

(**d**) (**e**) (**f**)

Figure 16. Correlation analysis of Lena before and after encryption. (**a**,**d**) horizontally adjacent, (**b**,**e**) vertically adjacent, (**c**,**f**) diagonally adjacent.

Table 8. Correlation coefficients of images.

Image	**Cipher Image**			**Plain Image**		
	Horizontal	**Verticall**	**Diagonal**	**Horizontal**	**Vertical**	**Diagonal**
Lena	−0.0008	0.0041	−0.0011	0.9753	0.9425	0.9180
Peppers	−0.0006	0.0052	−0.0043	0.9848	0.9906	0.9714
4.1.01	0.0010	−0.0016	−0.0123	0.9625	0.9672	0.9462
4.1.02	0.0045	−0.0012	−0.0121	0.9558	0.9312	0.8956
4.1.03	0.0017	0.0014	0.0068	0.9166	0.9729	0.9092
5.1.09	0.0035	−0.0023	−0.0037	0.9397	0.9008	0.9038
5.1.10	0.0042	−0.0052	0.0017	0.9399	0.9640	0.8977
5.1.11	0.0023	0.0021	−0.0020	0.8583	0.9061	0.8207
5.1.12	0.0006	−0.0108	0.0138	0.9750	0.9568	0.9367
5.1.13	−0.0019	0.0008	0.0028	0.8756	0.8750	0.7585
5.1.14	−0.0026	−0.0056	−0.0013	0.8962	0.9454	0.8540
6.1.01	0.0156	−0.0015	0.0071	0.9906	0.9872	0.9751

Table 9. Comparison on correlation coefficients for Lena.

Algorithms	**Horizontal**	**Vertical**	**Diagonal**
proposed	−0.0008	0.0041	−0.0011
Ref. [6]	−0.0209	0.0528	−0.0099
Ref. [16]	0.0058	−0.0024	0.0012
Ref. [51]	0.0082	−0.0032	−0.0025
Ref. [52]	0.0083	−0.0021	−0.0025
Ref. [53]	−0.0021	0.0009	0.0003
Ref. [54]	−0.0148	0.0106	0.0134

7.5. Information Entropy

Information entropy is an important indicator to describe the uncertainty of image information, which quantifies the distribution of the image's grayscale values [17]. Generally speaking, the higher the information entropy value, the higher the degree of disorder in the image [52]. The formula of information entropy is as follows.

$$H(s) = -\sum_{i=1}^{L} p(x_i)\log_2 p(x_i), \tag{28}$$

where L is the grayscale grade of the image,and $p(x_i)$ is the probability of the grayscale value x_i.

For 8-bit noise type grayscale images, the ideal value of information entropy is 8. The information entropy of different plain images and their corresponding cipher images are listed in Table 10. As can be seen, values of the information entropy of all encrypted images are close to 8. Table 11 lists the comparison results with other algorithms for Lena.

It is obvious that the proposed algorithm owns a larger information entropy compared with [6,16,51–54], which means the cipher images encrypted by the proposed algorithm have a stronger randomness. Thus, the proposed algorithm can resist statistical attacks based on entropy.

Table 10. Information entropy of images.

Image	Plain	Cipher
Lena	7.4116	7.9975
Peppers	7.7448	7.9970
4.1.01	7.0525	7.9973
4.1.02	6.4207	7.9972
4.1.03	5.5939	7.9975
5.1.09	6.7093	7.9976
5.1.10	7.3118	7.9973
5.1.11	6.4523	7.9971
5.1.12	6.7057	7.9970
5.1.13	1.5483	7.9974
5.1.14	7.3424	7.9972
6.1.01	7.2044	7.9975

Table 11. Information entropy comparison of Lena's cipher image.

Image	Proposed	[6]	[16]	[51]	[52]	[53]	[54]
Lena	7.9975	7.9661	7.9975	7.988	7.9971	7.9971	7.9975

7.6. Differential Attack Analysis

A secure image encryption algorithm should have excellent capability to resist differential attacks. Attackers can encrypt two slightly different plain images using the same algorithm, and then try to establish a link between the plain and cipher images by comparing the two encrypted images. The NPCR and UACI are able to evaluate whether encryption algorithms can resist differential attacks. The study in the literature [58] pointed out that the algorithm is resistant to differential attacks when the $NPCR > N_\alpha$ and $U_\alpha^- < UACI < U_\alpha^+$, where N_α, U_α^-, U_α^+ are the critical values and α is the significance level. The critical values for images of size 256 × 256 are listed in Table 12.

Table 12. The critical values of NPCR and UACI.

Images Size	NPCR%			UACI%		
	$N_{0.05}$	$N_{0.01}$	$N_{0.001}$	$(U_{0.05}^-, U_{0.05}^+)$	$(U_{0.01}^-, U_{0.01}^+)$	$(U_{0.001}^-, U_{0.001}^+)$
256 × 256	99.5693	99.5527	99.5341	(33.2824,33.6447)	(33.2255,33.7016)	(33.1594,7677)

To test the performance of the proposed algorithm against differential attacks, we randomly change a pixel value of the plain image to obtain the modified plain image. Subsequently, the two plain images are encrypted by the proposed algorithm to get the cipher images. The test is performed over 100 times with different test images. The mean values of the test results are listed in Tables 13 and 14, respectively. It can be seen that the proposed algorithm passes the test and is resistant to differential attacks. Table 15 lists a comparison of the NPCR and UACI values of Lena for different encryption algorithms. As can be seen, the NPCR and UACI values of Lena for the proposed algorithm are closer to the ideal value compared with [16,54], and the proposed algorithm has some merits compared with [51,53]. Thus, the proposed algorithm is capable of resisting differential attacks.

Table 13. NPCR test value.

Image	NPCR%	Critical NPCR%		
		$N_{0.05} = 99.5693\%$	$N_{0.01} = 99.5527\%$	$N_{0.001} = 99.5341\%$
Lena	99.6172	✓	✓	✓
Peppers	99.6086	✓	✓	✓
4.1.01	99.5892	✓	✓	✓
4.1.02	99.5793	✓	✓	✓
4.1.03	99.6002	✓	✓	✓
5.1.09	99.5998	✓	✓	✓
5.1.10	99.6052	✓	✓	✓
5.1.11	99.6175	✓	✓	✓
5.1.12	99.6134	✓	✓	✓
5.1.13	99.6100	✓	✓	✓
5.1.14	99.5895	✓	✓	✓
6.1.01	99.6213	✓	✓	✓
All black	99.5987	✓	✓	✓

Table 14. UACI test value.

Image	UACI%	Critical UACI%		
		$\mathcal{U}^{-}_{0.05} = 33.2824\%$ $\mathcal{U}^{+}_{0.05} = 33.6447\%$	$\mathcal{U}^{-}_{0.01} = 33.2255\%$ $\mathcal{U}^{+}_{0.01} = 33.7016\%$	$\mathcal{U}^{-}_{0.001} = 33.1594\%$ $\mathcal{U}^{+}_{0.001} = 33.7677\%$
Lena	33.4516	✓	✓	✓
Peppers	33.4752	✓	✓	✓
4.1.01	33.5487	✓	✓	✓
4.1.02	33.4870	✓	✓	✓
4.1.03	33.3864	✓	✓	✓
5.1.09	33.5019	✓	✓	✓
5.1.10	33.5172	✓	✓	✓
5.1.11	33.2873	✓	✓	✓
5.1.12	33.5091	✓	✓	✓
5.1.13	33.4249	✓	✓	✓
5.1.14	33.5100	✓	✓	✓
6.1.01	33.5516	✓	✓	✓
All black	33.4624	✓	✓	✓

Table 15. NPCR and UACI values of Lena for different algorithms.

Algorithms	NPCR%	UACI%
Proposed	99.6172	99.4516
Ref. [6]	-	-
Ref. [16]	99.60	33.45
Ref. [51]	99.6150	33.4205
Ref. [52]	-	-
Ref. [53]	99.9596	33.4588
Ref. [54]	99.5041	33.4238

7.7. Chosen/Known-Plaintext Attack Analysis

Chosen-plaintext and known-plaintext attacks are prevalent and high-threat types of attacks. The literature [59] indicated that an encryption algorithm with the capability to resist chosen-plaintext attacks can also resist known-plaintext attacks. Therefore, we only consider resisting chosen-plaintext attacks.

In the proposed algorithm, we exploit the SHA-512 hash values of the plain image to generate the system parameters and initial values of the chaotic system, making the proposed algorithm highly sensitive to the plain image. Thus, when attackers use the proposed algorithm to encrypt slightly changed plain images, the encryption result obtained is totally different. Attackers cannot gain the desired information using special images. Furthermore, we perform bit-level exclusive-or operations between different bit-planes. Attackers are incapable of using special images to simplify the diffusion process.

Attackers often use all-black or all-white plain images as special images to attack encryption algorithms, since such special images can disable the scrambling process [55]. We leverage the all-black and all-white plain images with the size 256 × 256 in the experiment, and the results are shown in Figure 17. It can be seen that the cipher images are noiselike images, and the histograms of the cipher images are quite flat. Attackers cannot derive valid information from the cipher images. Table 16 lists the χ^2 test results, information entropies, and correlation coefficients of the cipher images. It can be seen that the proposed algorithm has good encryption performance for all-white and all-black images. Therefore, the proposed algorithm can effectively resist chosen-plaintext and known-plaintext attacks.

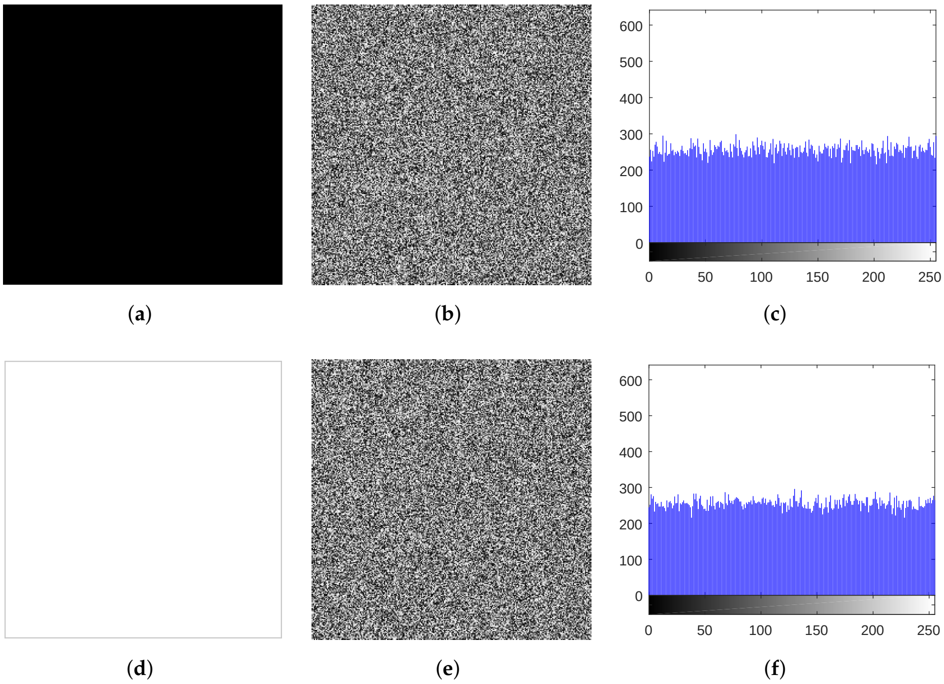

(**a**) (**b**) (**c**)

(**d**) (**e**) (**f**)

Figure 17. Experimental results of "all-black" and "all-white". (**a**) "all-black", (**b**) encryption "all-black", (**c**) histogram of encryption "all-black", (**d**) "all-white", (**e**) encryption "all-white", (**f**) histogram of encryption "all-white".

Table 16. Encryption results of all white and black images.

Cipher Image	χ^2 Test	Information Entropy	Correlation Coefficients		
			Horizontal	Vertical	Diagonal
All white	272.6641	7.9970	0.0008	−0.0005	0.0087
All black	253.8516	7.9972	−0.0012	−0.0019	0.0116

7.8. Cropping Attack and Noise Attack Analysis

In the actual transmission process of the network, the images are at high risk of data loss or noise contamination. Therefore, a secure image encryption algorithm shall be robust against cropping attacks and noise. Take "Lena" as a test image. The cropped images are shown in Figure 18a–d. We can see that even if cropping attacks on cipher images lead to data loss, the decrypted image can still be recognized by the human eye. This shows that the proposed algorithm is resistant to cropping attacks.

To test the antinoise performance of the proposed algorithm, we add salt and pepper noise with different intensities to the cipher image, where the intensities are 0.01, 0.05, and 0.1, respectively. The results are shown in Figure 19a–c. It can be seen that the decrypted images contain some noises, but we can still recognize most of the information in the plain image by human eyes. The proposed algorithm is resistant to noise attacks. In addition, as shown in Figure 19d, salt and pepper noise with intensity of 0.05 is added to the cipher image with 6.25% cropping. The decrypted image Figure 19h can still be recognized by human eyes. Thus, the proposed algorithm can effectively resist cropping attacks and noise attacks.

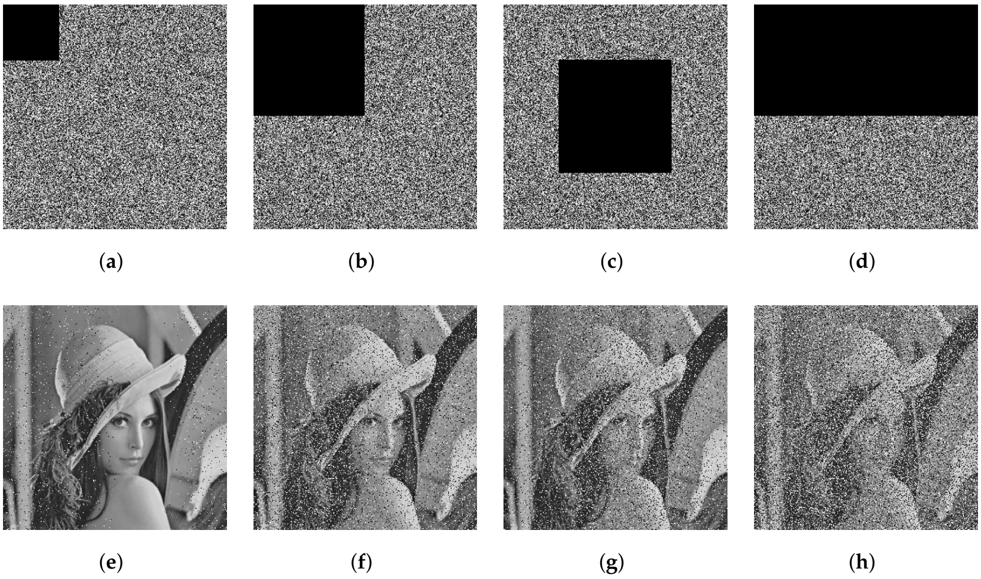

Figure 18. The results of cropping attack. (**a**) Encrypted image with 6.25% cropping, (**b**) encrypted image with 25% cropping, (**c**) encrypted image with 25% cropping (middle), (**d**) encrypted image with 50% cropping, (**e**) decryption of (**a**), (**f**) decryption of (**b**), (**g**) decryption of (**c**), and (**h**) decryption of (**d**).

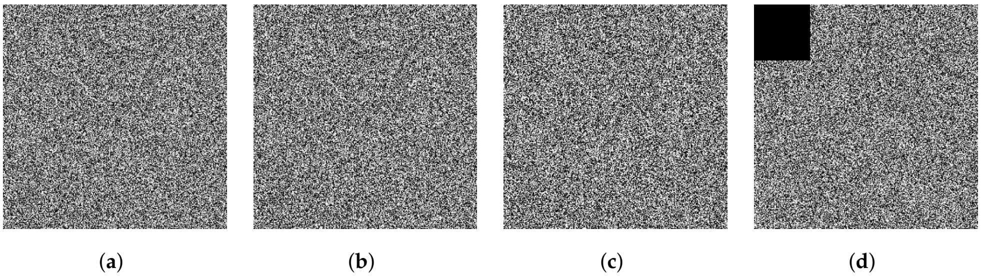

Figure 19. *Cont.*

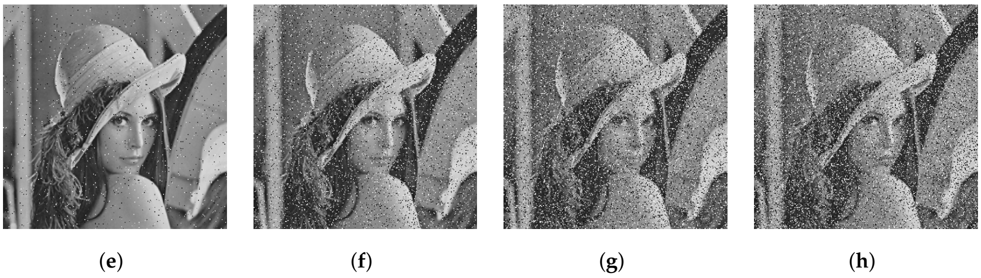

(**e**) (**f**) (**g**) (**h**)

Figure 19. The results of noise attack. (**a**) Encrypted image with 0.01 salt & pepper noise, (**b**) encrypted image with 0.05 salt & pepper noise, (**c**) encrypted image with 0.1 salt & pepper noise, (**d**) encrypted image with 0.05 salt & pepper noise and 6.25% clipping, (**e**) decryption of (**a**), (**f**) decryption of (**b**), (**g**) decryption of (**c**), and (**h**) decryption of (**d**).

8. Conclusions

In this paper, we develop a hybrid domain image encryption algorithm based on improved Henon map. First, we construct an improved Henon map called 2D-ICHM, and dynamical analysis indicates that it has excellent chaotic properties. Second, an image encryption algorithm with a double sandwich structure is proposed using 2D-ICHM, where the content structure of the image is destroyed by the proposed chunking–arrangement–combination operation, which enhances the security performance of the algorithm. Third, the SHA-512 hash value of the plain image is used to obtain the initial values and system parameters of the chaotic system, which enhances the plaintext sensitivity. Simulation experiments and security analysis show that the proposed image encryption algorithm has a huge key space, strong key sensitivity, and strong robustness to various cryptanalytic attacks. Therefore, the proposed algorithm has high level of security.

However, the limitations of this algorithm include the inability to encrypt color images directly and the unsuitability for real-time confidential communications. We will extend our approach based on the ideas of the block and nature-inspired optimization techniques from the literature [60] to address these shortcomings in future research. Considering the excellent properties of hyperchaotic systems, we try to design a 2D hyperchaotic system for image encryption. In the last few years, machine learning and deep learning networks have shown great advantages in the field of image processing. We attempt to introduce these techniques to simplify and improve the proposed double sandwich encryption structure to design a real-time secure color image encryption algorithm.

Author Contributions: Conceptualization, Y.C. and S.X.; methodology, Y.C. and S.X.; software, Y.C.; validation, Y.C., S.X. and J.Z.; formal analysis, Y.C.; investigation, S.X.; resources, Y.C.; data curation, Y.C.; writing—original draft preparation, Y.C.; writing—review and editing, S.X. and J.Z.; visualization, Y.C. and J.Z.; supervision, S.X.; project administration, Y.C. and S.X. All authors have read and agreed to the published version of the manuscript.

Funding: This research received no external funding.

Institutional Review Board Statement: Not applicable.

Informed Consent Statement: Not applicable.

Data Availability Statement: Data sharing not applicable.

Acknowledgments: We gratefully acknowledge the reviewers for their comments and suggestions.

Conflicts of Interest: The authors declare no conflict of interest.

Abbreviations

The following abbreviations are used in this manuscript:

IWT	Integer wavelet transform
DNA	Deoxyribonucleic acid
SHA-512	Secure hash algorithm-512
DES	Data Encryption Standard
AES	Advanced Encryption Standard
LSTM-ANN	Long short-term memory artificial neural networks
GAN	Generative adversarial network
CNN	Convolutional neural network
1D	One-dimensional
2D	Two-dimensional
HD	High-dimensional
2D-CHM	Classical two-dimensional Henon map
2D-ICHM	Improved classical two-dimensional Henon map
2D-SM	Two-dimensional sine map
IHM	Improved Henon map
QR	Qatari Rial
ApEn	Approximate entropy
LE	Lyapunov exponent
A	Adenine
C	Cytosine
G	Guanine
T	Thymine
NPCR	Number of pixels change rate
UACI	Unified average changing intensity

References

1. Kanso, A.; Ghebleh, M. An efficient and robust image encryption scheme for medical applications. *Commun. Nonlinear Sci. Numer. Simul.* **2015**, *24*, 98–116. [CrossRef]
2. El-Shafai, W.; Khallaf, F.; El-Rabaie, E.S.M.; El-Samie, F.E.A. Robust medical image encryption based on DNA-chaos cryptosystem for secure telemedicine and healthcare applications. *J. Ambient. Intell. Humaniz. Comput.* **2021**, *12*, 9007–9035. [CrossRef]
3. Aashiq, B.S.; Amirtharajan, R. A robust medical image encryption in dual domain: Chaos-DNA-IWT combined approach. *Med. Biol. Eng. Comput.* **2020**, *58*, 1445–1458.
4. Hedayati, R.; Mostafavi, S. A Lightweight Image Encryption Algorithm for Secure Communications in Multimedia Internet of Things. *Wirel. Pers. Commun.* **2021**, 1–23. doi:10.1007/s11277-021-09173-w. [CrossRef]
5. Singh, S.P.; Bhatnagar, G. A Novel Biometric Inspired Robust Security Framework for Medical Images. *IEEE Trans. Knowl. Data Eng.* **2021**, *33*, 810–823. [CrossRef]
6. Sang, Y.; Sang, J.; Alam, M.S. Image encryption based on logistic chaotic systems and deep autoencoder. *Pattern Recognit. Lett.* **2022**, *153*, 59–66. [CrossRef]
7. Liu, H.; Wang, X. Color image encryption based on one-time keys and robust chaotic maps. *Comput. Math. Appl.* **2010**, *59*, 3320–3327. [CrossRef]
8. Li, Y.; Wang, C.; Chen, H. A hyper-chaos-based image encryption algorithm using pixel-level permutation and bit-level permutation. *Opt. Lasers Eng.* **2017**, *90*, 238–246. [CrossRef]
9. Zhao, H.; Xie, S.; Zhang, J.; Wu, T. A dynamic block image encryption using variable-length secret key and modified Henon map. *Optik* **2021**, *230*, 166307. [CrossRef]
10. Zhao, Z.-P.; Zhou, S.; Wang, X.Y. A new chaotic signal based on deep learning and its application in image encryption. *Acta Phys. Sin* **2021**, *70*, 23. [CrossRef]
11. Chai, X.; Tian, Y.; Gan, Z.; Lu, Y.; Wu, X.J.; Long, G. A robust compressed sensing image encryption algorithm based on GAN and CNN. *J. Mod. Opt.* **2021**, *69*, 1–18. doi:10.1080/09500340.2021.2002450. [CrossRef]
12. Sreelakshmi, K.; Ravi, R.V. An Encryption-then-Compression Scheme Using Autoencoder Based Image Compression for Color Images. In Proceedings of the 2020 7th International Conference on Smart Structures and Systems (ICSSS), Chennai, India, 23–24 July 2020; pp. 1–5.
13. Abdullah, A.H.; Enayatifar, R.; Lee, M. A hybrid genetic algorithm and chaotic function model for image encryption. *AEUE Int. J. Electron. Commun.* **2012**, *66*, 806–816. [CrossRef]
14. Mansouri, A.; Wang, X. A novel one-dimensional chaotic map generator and its application in a new index representation-based image encryption scheme. *Inf. Sci.* **2021**, *563*, 91–110. [CrossRef]

15. Raza, S.F.; Satpute, V. A novel bit permutation-based image encryption algorithm. *Nonlinear Dyn.* **2019**, *95*, 859–873. [CrossRef]
16. Li, X.; Mou, J.; Xiong, L.; Wang, Z.; Xu, J. Fractional-order double-ring erbium-doped fiber laser chaotic system and its application on image encryption. *Opt. Laser Technol.* **2021**, *140*, 107074. [CrossRef]
17. Wang, T.; Wang, M.H. Hyperchaotic image encryption algorithm based on bit-level permutation and DNA encoding. *Opt. Laser Technol.* **2020**, *132*, 106355. [CrossRef]
18. Suri, S.; Vijay, R. A Pareto-optimal evolutionary approach of image encryption using coupled map lattice and DNA. *Neural Comput. Appl.* **2020**, *32*, 11859–11873. [CrossRef]
19. Xie, Y.; Yu, J.; Guo, S.; Ding, Q.; Wang, E. Image encryption scheme with compressed sensing based on new three-dimensional chaotic system. *Entropy* **2019**, *21*, 819. [CrossRef]
20. Wang, X.; Liu, C.; Jiang, D. A novel triple-image encryption and hiding algorithm based on chaos, compressive sensing and 3D DCT. *Inf. Sci.* **2021**, *574*, 505–527. [CrossRef]
21. Thanikaiselvan, V.; Mantripragada, N.; Singh, A.P.; Bhasin, N. Encrypting Multiple Images using Stacked Autoencoders. In Proceedings of the 2019 International Conference on Vision Towards Emerging Trends in Communication and Networking (ViTECoN), Vellore, India, 30–31 March 2019; pp. 1–6.
22. Suhail, K.A.; Sankar, S. Image Compression and Encryption Combining Autoencoder and Chaotic Logistic Map. *Iran. J. Sci. Technol. Trans. A Sci.* **2020**, *44*, 1091–1100. [CrossRef]
23. Gong, L.; Deng, C.; Pan, S.; Zhou, N. Image compression-encryption algorithms by combining hyper-chaotic system with discrete fractional random transform. *Opt. Laser Technol.* **2018**, *103*, 48–58. [CrossRef]
24. Belazi, A.; El-Latif, A.A.; Diaconu, A.V.; Rhouma, R.; Belghith, S. Chaos-based partial image encryption scheme based on linear fractional and lifting wavelet transforms. *Opt. Lasers Eng.* **2017**, *88*, 37–50. [CrossRef]
25. Luo, Y.; Du, M.; Liu, J. A symmetrical image encryption scheme in wavelet and time domain. *Commun. Nonlinear Sci. Numer. Simul.* **2015**, *20*, 447–460. [CrossRef]
26. Li, X.; Meng, X.; Yang, X.; Wang, Y.; Yin, Y.; Peng, X.; He, W.; Dong, G.; Chen, H. Multiple-image encryption via lifting wavelet transform and XOR operation based on compressive ghost imaging scheme. *Opt. Lasers Eng.* **2018**, *102*, 106–111. [CrossRef]
27. Fan, C.; Ding, Q. A novel image encryption scheme based on self-synchronous chaotic stream cipher and wavelet transform. *Entropy* **2018**, *20*, 445. [CrossRef]
28. Farah, M.B.; Guesmi, R.; Kachouri, A.; Samet, M. A novel chaos based optical image encryption using fractional Fourier transform and DNA sequence operation. *Opt. Laser Technol.* **2020**, *121*, 105777. [CrossRef]
29. Hua, Z.; Zhu, Z.; Chen, Y.; Li, Y. Color image encryption using orthogonal Latin squares and a new 2D chaotic system. *Nonlinear Dyn.* **2021**, *104*, 4505–4522. [CrossRef]
30. Zhang, Y. The fast image encryption algorithm based on lifting scheme and chaos. *Inf. Sci.* **2020**, *520*, 177–194. [CrossRef]
31. Hirsch, M.W.; Smale, S.; Devaney, R.L. *Differential Equations, Dynamical Systems, and an Introduction to Chaos*; Elsevier: Amsterdam, The Netherlands, 2012.
32. Chen, G.; Mao, Y.; Chui, C.K. A symmetric image encryption scheme based on 3D chaotic cat maps. *Chaos Solitons Fractals* **2004**, *21*, 749–761. [CrossRef]
33. Fridrich, J. Symmetric ciphers based on two-dimensional chaotic maps. *Int. J. Bifurc. Chaos* **1998**, *8*, 1259–1284. [CrossRef]
34. Hua, Z.; Zhou, Y.; Pun, C.M.; Chen, C.P. 2D Sine Logistic modulation map for image encryption. *Inf. Sci.* **2015**, *297*, 80–94. [CrossRef]
35. Zhu, H.; Zhao, Y.; Song, Y. 2D logistic-modulated-sine-coupling-logistic chaotic map for image encryption. *IEEE Access* **2019**, *7*, 14081–14098. [CrossRef]
36. Bao, H.; Hua, Z.; Wang, N.; Zhu, L.; Chen, M.; Bao, B. Initials-Boosted Coexisting Chaos in a 2D Sine Map and Its Hardware Implementation. *IEEE Trans. Ind. Inform.* **2020**, *17*, 1132–1140. [CrossRef]
37. Gao, X. A color image encryption algorithm based on an improved Hénon map. *Phys. Scr.* **2021**, *96*, 065203. [CrossRef]
38. Hénon, M. A two-dimensional mapping with a strange attractor. In *The Theory of Chaotic Attractors*; Springer: Berlin, Germany, 1976; pp. 94–102.
39. Wolf, A.; Swift, J.B.; Swinney, H.L.; Vastano, J.A. Determining Lyapunov exponents from a time series. *Phys. D Nonlinear Phenom.* **1985**, *16*, 285–317. [CrossRef]
40. Dieci, L.; Vleck, E.S.V. Perturbation Theory for Approximation of Lyapunov Exponents by QR Methods. *J. Dyn. Differ. Equ.* **2006**, *18*, 815–840. [CrossRef]
41. Wang, C.; Ding, Q. A new two-dimensional map with hidden attractors. *Entropy* **2018**, *20*, 322. [CrossRef]
42. Pincus, S.M. Approximate entropy as a measure of system complexity. *Proc. Natl. Acad. Sci. USA* **1991**, *88*, 2297–2301. [CrossRef]
43. Rukhin, A.; Soto, J.; Nechvatal, J.; Smid, M.; Barker, E.; Leigh, S.; Levenson, M.; Vangel, M.; Banks, D.; Heckert, A.; et al. *A Statistical Test Suite for Random and Pseudorandom Number Generators for Cryptographic Applications*; Technical Report; Booz-Allen and Hamilton Inc.: McLean, VA, USA, 2001.
44. Gottwald, G.A.; Melbourne, I. Testing for chaos in deterministic systems with noise. *Phys. D Nonlinear Phenom.* **2005**, *212*, 100–110. [CrossRef]
45. Zhu, S.; Zhu, C. Security Analysis and Improvement of an Image Encryption Cryptosystem Based on Bit Plane Extraction and Multi Chaos. *Entropy* **2021**, *23*, 505. [CrossRef]

46. Wen, H.; Yu, S. Cryptanalysis of an image encryption cryptosystem based on binary bit planes extraction and multiple chaotic maps. *Eur. Phys. J. Plus* **2019**, *134*, 1–16. [CrossRef]
47. Daubechies, I.; Sweldens, W. Factoring wavelet transforms into lifting steps. *J. Fourier Anal. Appl.* **1998**, *4*, 247–269. [CrossRef]
48. Chen, H.; Liu, Z.; Zhang, H. Study on Scalable Coding Algorithm for Medical Image. In Proceedings of the 2005 IEEE Engineering in Medicine and Biology 27th Annual Conference, Shanghai, China, 17–18 January 2006; pp. 6360–6363.
49. Jin, X.; Duan, X.; Jin, H.; Ma, Y. A novel hybrid secure image encryption based on the shuffle algorithm and the hidden attractor chaos system. *Entropy* **2020**, *22*, 640. [CrossRef] [PubMed]
50. Alvarez, G.; Li, S. Some basic cryptographic requirements for chaos-based cryptosystems. *Int. J. Bifurc. Chaos* **2006**, *16*, 2129–2151. [CrossRef]
51. ElKamchouchi, D.H.; Mohamed, H.G.; Moussa, K.H. A bijective image encryption system based on hybrid chaotic map diffusion and DNA confusion. *Entropy* **2020**, *22*, 180. [CrossRef] [PubMed]
52. Wang, X.; Chen, S.; Zhang, Y. A chaotic image encryption algorithm based on random dynamic mixing. *Opt. Laser Technol.* **2021**, *138*, 106837. [CrossRef]
53. Wang, X.; Wang, Y.; Zhu, X.; Luo, C. A novel chaotic algorithm for image encryption utilizing one-time pad based on pixel level and DNA level. *Opt. Lasers Eng.* **2020**, *125*, 105851. [CrossRef]
54. Zhang, Y. A new unified image encryption algorithm based on a lifting transformation and chaos. *Inf. Sci.* **2021**, *547*, 307–327. [CrossRef]
55. Zhang, Y.; Zhang, L.; Zhong, Z.; Yu, L.; Shan, M.; Zhao, Y. Hyperchaotic image encryption using phase-truncated fractional Fourier transform and DNA-level operation. *Opt. Lasers Eng.* **2021**, *143*, 106626. [CrossRef]
56. Zhang, Y. Plaintext Related Image Encryption Scheme Using Chaotic Map. *Indones. J. Electr. Eng. Comput. Sci.* **2014**, *12*, 635–643. [CrossRef]
57. Yang, Y.; Wang, L.; Duan, S.; Luo, L. Dynamical analysis and image encryption application of a novel memristive hyperchaotic system. *Opt. Laser Technol.* **2021**, *133*, 106553. [CrossRef]
58. Wu, Y.; Noonan, J.P.; Agaian, S. NPCR and UACI randomness tests for image encryption. *Cyber J. Multidiscip. J. Sci. Technol. J. Sel. Areas Telecommun. (JSAT)* **2011**, *1*, 31–38.
59. Ravichandran, D.; Praveenkumar, P.; Rayappan, J.B.B.; Amirtharajan, R. Chaos based crossover and mutation for securing DICOM image. *Comput. Biol. Med.* **2016**, *72*, 170–184. [CrossRef] [PubMed]
60. Singh, P.; Devi, K.J.; Thakkar, H.K.; Santamaría, J. Blind and Secured Adaptive Digital Image Watermarking Approach for High Imperceptibility and Robustness. *Entropy* **2021**, *23*, 1650. [CrossRef] [PubMed]